J. Fluid Mech. (1987), *vol.* 174, *pp.* 271–298
Printed in Great Britain

Large-scale vortex structures in turbulent wakes behind bluff bodies. Part 2. Far-wake structures

By T. R. STEINER AND A. E. PERRY
Department of Mechanical Engineering, University of Melbourne, Parkville, 3052, Victoria, Australia

(Received 30 July 1985 and in revised form 12 May 1986)

An investigation of a selection of high-Reynolds-number bluff-body flows was conducted. Here in Part 2 phase-averaged velocity-field results will be presented for several far-wake flows generated by nominally two-dimensional and three-dimensional bodies. In these far-wake flows the shed vortices have approached a nearly constant convection velocity. Some mean velocity and phase-averaged and global Reynolds-stress measurements are also presented. The turbulent wake of a lift-producing three-dimensional body has been examined. Also included are the phase-averaged wake patterns behind a flapping flag and a windmill. The topological structure of these patterns is discussed and a preliminary classification of wake patterns is presented.

1. Introduction

From earlier work carried out with periodic laminar-flow eddying motions a classification of smoke patterns has been made for some simple cases (e.g. see Perry & Lim 1978). From work presented here a more complete classification has emerged and this is shown in figure 1. These are the conjectured periodic laminar-flow analogues for the flows observed here. Of course, with high-Reynolds-number flows the smoke patterns would have fine-scale eddying motions superimposed on them, and the frequency and scale of the large-scale motions would possess a degree of randomness. It is conjectured that these sketches represent the streakline patterns that one would obtain if the phase-averaged velocity fields were integrated in time (or phase) and the effects of turbulent diffusion were not taken into account. These should bear a resemblance to actual smoke patterns. Such integrations have not yet been carried out, nor have all cases here been observed with smoke because of the difficulties of high-Reynolds-number flow visualization.

Unless otherwise indicated all measurements were taken in a vertical nominal plane of symmetry. The spatial coordinates in this plane are x and y for the streamwise and vertical cross-stream directions respectively. The corresponding velocities are denoted u and v. The spanwise direction and velocity component will be denoted z and w respectively.

2. Some difficulties in phase detection

In the case of three-dimensional bodies (particularly the elliptical planform) phase detection as described in Part 1 (Perry & Steiner 1986) gave problems with an excessive number of false phase pulses being generated. It was discovered that the power-spectral density of the signal from the stationary phase-detection hot-wire had a number of peaks of similar magnitude spaced about an octave apart. Only one peak

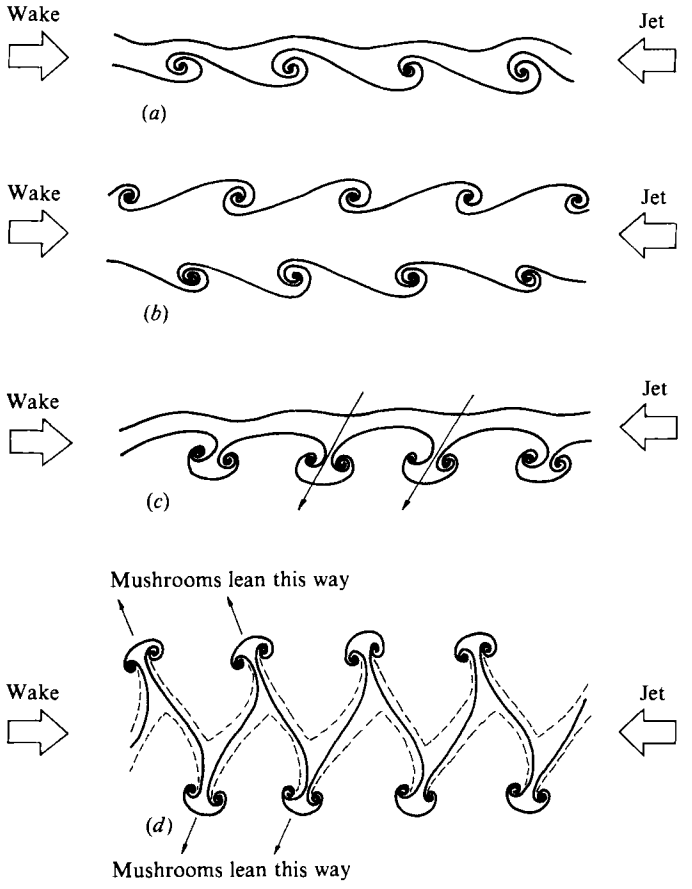

FIGURE 1. Classification of simple smoke-pattern structures (streamwise growth not shown). (*a*) Single-sided 'loop' structure; (*b*) double-sided 'loop' structure; (*c*) single-sided 'mushroom' structure, (*d*) double-sided 'mushroom' structure.

corresponded to the 'true' vortex-shedding frequency and the other peaks caused confusion in the phase detection. By notch filtering with a 1/3 octave bandwidth filter and varying the centre frequency, it was found that an organized waveform of velocity as a function of streamwise distance and phase was produced only when the signal was filtered at a frequency corresponding to one particular peak in the spectrum. Other peaks yielded a complete absence of 'structure'.

It is felt that the peak one octave lower than the 'true' peak was associated with vortex shedding in a plane normal to the plane being investigated. However, this is not conclusive from the cursory tests carried out.

3. Determination of phase velocity

Work by Perry, Chong & Lim (1982) and Steiner (1984) showed how differently translating observers may interpret distinctly different streamline patterns in the same flow. This kind of ambiguity makes it extremely important to determine with reasonable accuracy the correct convection velocity of the part of the flow that is

of interest. This is especially important where developing flows are encountered, as misinterpretation of sections of the flow not viewed at the appropriate velocity may lead to a gross misunderstanding of the physical processes involved.

In order to understand how this 'appropriate' reference frame is determined it is useful to know how velocity vector fields are assembled. As the probe was propelled upstream along the working section, the signals from the two hot-wire channels were sampled using a PDP 11/10 digital computer. This was fitted with a 'Laboratory Peripheral System' which contained an 8-channel A/D converter, among other items of hardware. The converted voltages were then allocated positions in a two-dimensional array in the computer's memory. One dimension of this array corresponded to the position at which the sample was taken within the wind tunnel, and the other dimension corresponded to the phase of the vortex-shedding cycle at the time when the sample was taken. For the purposes of this work each vortex-shedding cycle was divided into sixteen discrete intervals or 'phases'. Running totals were kept in each phase-position location for subsequent averaging. This is referred to as averaging the data on the basis of phase. By applying the nonlinear calibration equations to these averaged voltages it was possible to obtain the phase-averaged velocities at many streamwise locations along one given horizontal level. It is possible to average in this way since the spread of sample values within individual phase-position locations is small. This was verified by Watmuff (1979). After traversing the probe and repeating the process of data acquisition along other levels, entire velocity vector fields could be assembled.

It is difficult to precisely define the convection velocity, phase velocity, or celerity of a coherent structure, especially when the pattern is distorting so that different parts of the pattern move relative to one another. One possible approach follows from the notion that if an observer moves with the pattern, then that pattern will appear to be more steady than if it were being viewed in any other translating reference frame. That is, the most appropriate translating reference frame for observation would be the one in which the pattern retains the highest degree of correlation with itself as time (or phase) progresses. This would correspond to the phase velocity of the pattern.

Figure 2 shows a surface of the value of cross-stream velocity v for one level plotted as a function of streamwise distance x and phase ϕ. The surface has waves that suggest the existence of a characteristic direction. Below the surface plot are shown the views of $v(x)$ at fixed phases that an observer would see by looking at the surface along different directions. These 'lines of sight' all lie parallel to the (x, ϕ)-plane. It is clear that the degree of collapse of the distributions of velocity with streamwise distance at *different fixed phases* changes with the viewing angle. This degree of collapse was optimized by a correlation-coefficient method similar to that described by Perry & Tan (1984). The resulting value of $\mathrm{d}x/\mathrm{d}\phi$, the slope of the viewing line that leads to maximum correlation coefficient, is related to the convection velocity U_c by $U_c = 16f\,\mathrm{d}x/\mathrm{d}\phi$, where ϕ is the phase defined as a dimensionless number varying between 0 and 16 over one vortex-shedding cycle, and f is the mean frequency of vortex shedding in Hz.

The value of convection velocity estimated in this way usually differed between levels by a few percent since the structures were still undergoing a continuous distortion. The values of convection velocity determined in this way using data at levels near to the centres of eddies were used when the fields were being plotted since it was felt that these would be the most meaningful for the purpose of viewing the patterns.

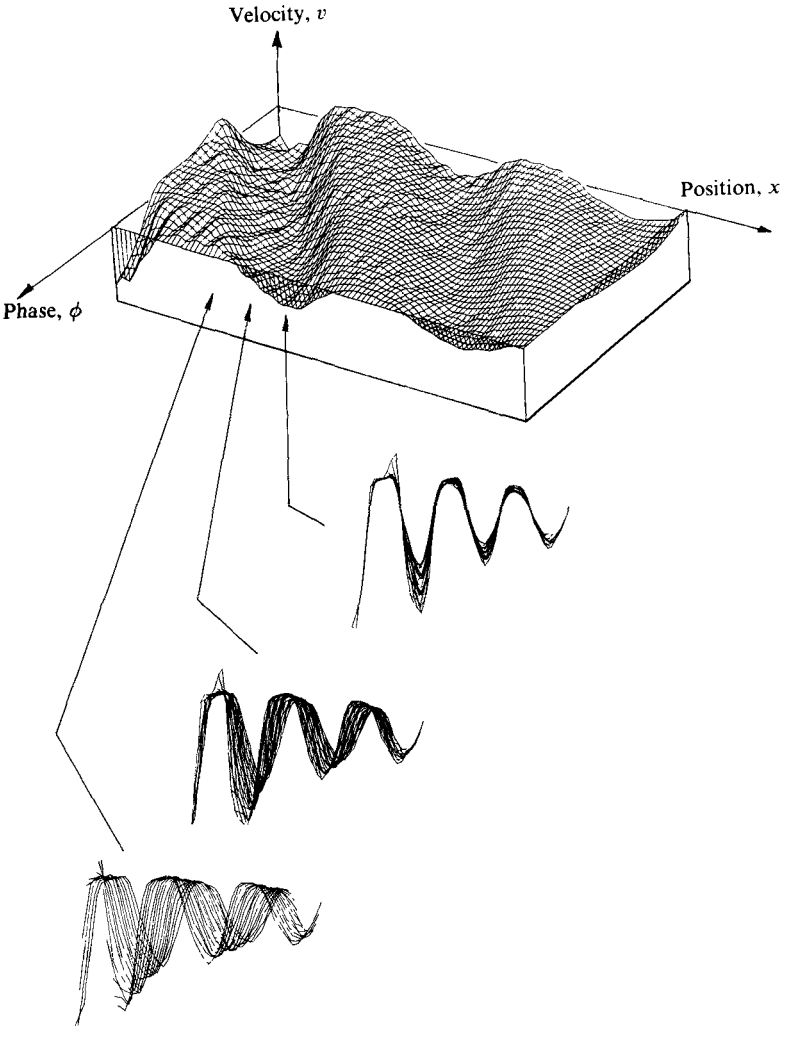

FIGURE 2. Typical surface plot of velocity as a function of phase and streamwise distance. Also shown are views of $v(x)$ at fixed phases as seen by different observers.

4. Experimental results

The flying-hot-wire apparatus and techniques used to perform these experiments have been described in Part 1 (Perry & Steiner 1986). Phase-averaged velocity-vector fields and the corresponding integrated phase-averaged streamline patterns are presented for the flow behind several bodies. The cases presented are: (i) a nominally two-dimensional flat plate placed normal to the free-stream flow; (ii) a nominally two-dimensional flat plate placed at an angle of attack of 45° to the free-stream flow; (iii) an elliptical planform at an angle of attack of 60°; (iv) a flapping flag; (v) a propeller being operated as a windmill.

The values of some relevant experimental parameters are listed in table 1. The techniques used to gather experimental data and produce the various vector fields and integrated streamline patterns have already been discussed in Part 1. The results presented here are for the region of the wakes extending further downstream than

Case	Experiment	Reynolds number and relevant lengthscale (l)	$St = \frac{fl}{U_\infty}$	$\frac{U_c}{U_\infty}$	Blockage ratio	U_∞ m/s
1	Far-wake 2-D normal body (no end plates fitted)	19900 – Projected height (0.10 m)	0.170	0.80	0.246	2.974
2	Far-wake 2-D inclined body (no end plates fitted)	13300 – Projected height (0.071 m)	0.161	0.78	0.174	2.859
3	Elliptical planform (angle of attack = 60°)	11500 – Minor axis length (chord length 0.04 m)	0.148	0.83	0.006	4.328
4	Flapping flag	15900 – Flag length (0.067 m)	0.35	0.99	—	3.614
5	Propeller wake	37900 – Propeller blade diameter (0.155 m)	0.313	0.83	0.021	3.585

TABLE 1. Some experimental parameters: St is the Strouhal number where f is the frequency in Hz of vortex shedding, and U_c is the convection velocity of the eddying motions about five lengthscales downstream of the body

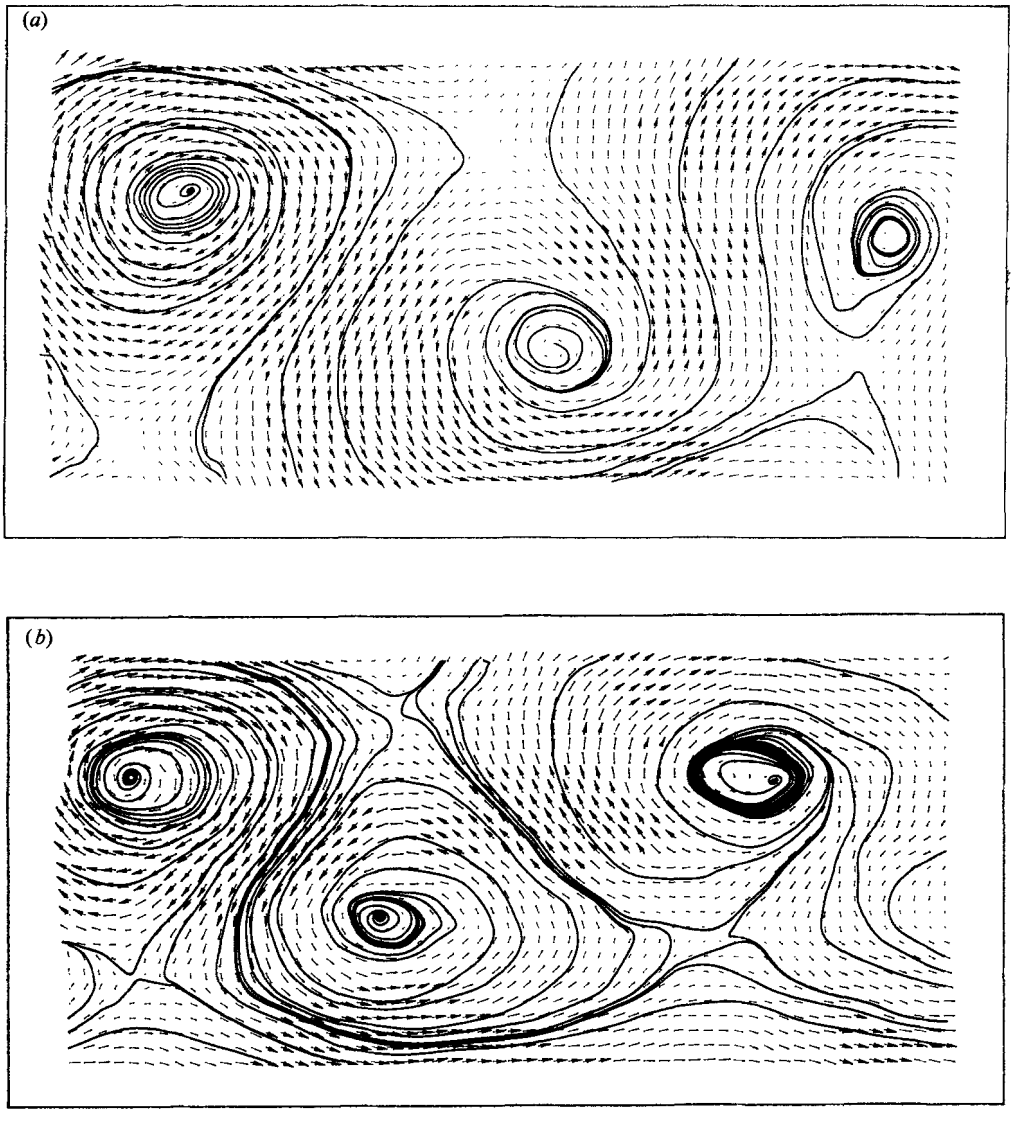

FIGURE 3. Velocity field and integrated streamline pattern for one representative phase in the far-wake behind (*a*) the normal bluff plate and (*b*) the inclined bluff plate.

at least four body lengthscales from the models. In all fields presented, the free-stream flow is represented as being from left to right.

4.1. *Nominally two-dimensional bluff-body cases*

Typical phase-averaged velocity vector fields for the far wakes of the nominally two-dimensional bluff body placed normal to the free-stream and also at an angle of attack are given in figures 3(*a*, *b*) respectively. For these measurements no end plates were attached to the body and its ends were butted up against the wind-tunnel walls. The vectors furthest to the left were measured at stations five and seven heights downstream from the body in figures 3(*a*, *b*) respectively.

Both patterns resemble the classical Kármán vortex street, although the three-

dimensional nature of this real flow leads to the appearance of foci rather than centres. In figure 1, Part 1 a 'pictorial dictionary' of a number of flow pattern features is provided.

The vortex-spacing ratio (vortex space to row separation) is approximately 0.17 for the normal bluff plate and 0.21 for the same plate at an angle of attack. It is believed that the main reason for this difference is the change in area-blockage ratio that existed between the two flow cases.

There do not appear to be any significant differences in topological structure between the two wake flows, but rather only changes in streamwise and cross-stream lengthscales. The topological similarity of these two flows is a consequence of the two-dimensional nature of the bluff plate. As there were no free ends for simple isolated trailing vortices to form around when the bluff body was placed at an angle of attack, the vortex system which characterizes the flow could not change. It is of course true that horseshoe vortices would form at the junctions of the body and the wind-tunnel walls, but it may be considered that they lie very close to their image vortices and so the far-field influence of these vortex-filament pairs would be small.

When viewed at the correct velocity, the far-wake eddies of these two flow cases generally appear as 'limit cycle' patterns which are unstable in the large (see figure 1, Part 1). Limit cycles have been discussed in some detail in Part 1 and will be examined further here in §4. Here the term 'unstable' refers to the type of behaviour where streamlines diverge away from the 'bifurcation line'. The existence of such two-celled flow indicates that there are regions of coaxial positive and negative strain. One conjectured explanation for this highly organized form of three-dimensional behaviour is that an initially straight vortex filament which develops a kink along its length will have an induced velocity field which may lead to the appearance of limit cycles. Such a vortex filament could develop a 'bi-helical deformation' of the type suggested in §4 of Part 1.

4.2. *The cone-angle problem and the measurement of velocity components in highly turbulent flows*

Tutu & Chevray (1975), and later Kawall, Shokr & Keffer (1983), analysed the response of hot-wire probes placed in highly turbulent flows. They examined the effect on the inferred velocity components and turbulent stresses due to a significant component of velocity acting normal to the measuring plane of a cross-wire probe. They also considered the effect of so-called 'rectification' of the components of the velocity vector that lie in the plane of the probe, when the turbulence intensity is significant. They found that these conditions may lead to large errors in inferred mean velocity, and Reynolds normal and shear stresses.

The calibration technique used here was the dynamic method described in Perry (1982) where a third-order polynomial is fitted to the static calibration data using coefficients obtained from a second-order fit to the dynamically determined sensitivities. Perry *et al.* (1983) found that this calibration technique yields accurate results provided that the velocity vectors relative to the probe are contained within a conical type of envelope of limited angle. The total included angle of this cone through the measuring plane of the probe needs to be less than 40° when using crossed wires with an included angle of 90° facing the flow. In the plane normal to this, the allowable included angle of the cone is of the same order. In this experiment the actual spanwise velocity fluctuations are of the same order or less than the vertical cross-stream velocity fluctuations.

Figures 4(*a*, *b*) show some inferred velocity vectors in an experimental situation

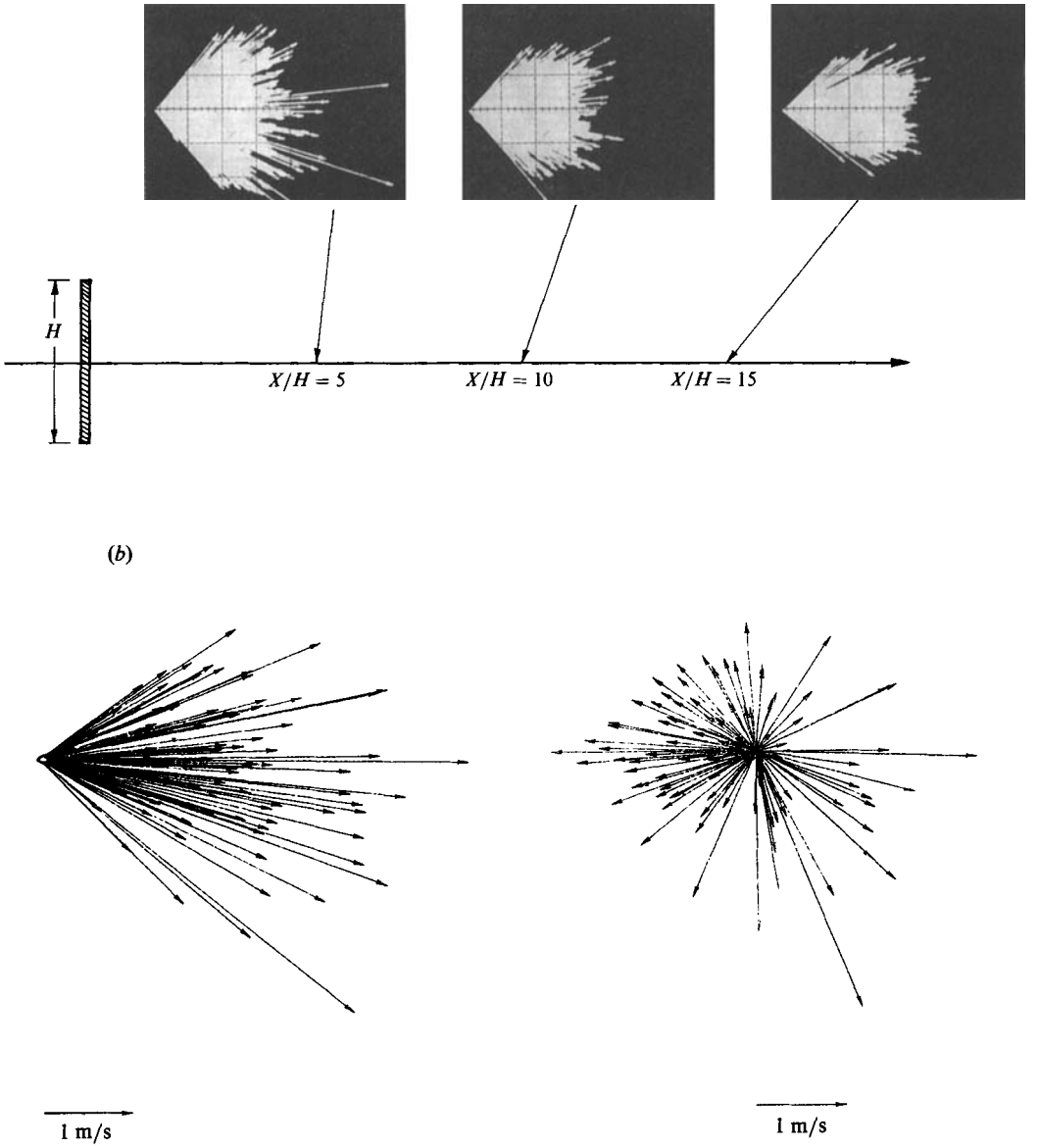

FIGURE 4. (*a*) Velocity vectors in the wake of a two-dimensional bluff plate. Velocities were inferred using a stationary hot-wire probe with 100° wire angle. (*b*) The effect of 'flying' the wires. Velocity vectors relative to a flying hot-wire (left), and relative to the stationary body (right) (velocity data accumulated at $X/H = 1$). This data is from the case where non-phase-averaged information was required. In this case the probe was not given a sufficient bias velocity.

and it can be seen that with this stationary probe the cone angle of vector directions is large. This would lead to large errors. These problems can be overcome by 'flying' the wires. On the left-hand side of figure 4(*b*) are velocity vectors inferred relative to a moving probe at a station close to the same bluff body. These vectors relative to the probe are now confined to a cone of much smaller included angle. Subtracting the known bias velocity leaves us with the true velocities relative to the stationary

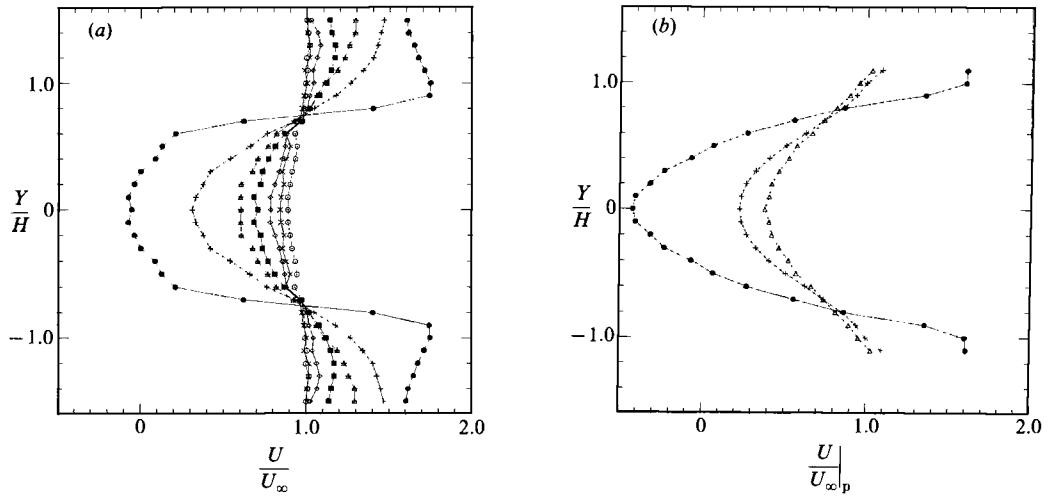

FIGURE 5. Temporal mean velocity profiles sampled behind normal bluff body with no end plates attached: (*a*) global data; (*b*) phase-averaged data (suffix p). ●, $X/H = 1$; +, 3; △, 5; ■, 7; ◇, 9; ×, 11; ○, 13.

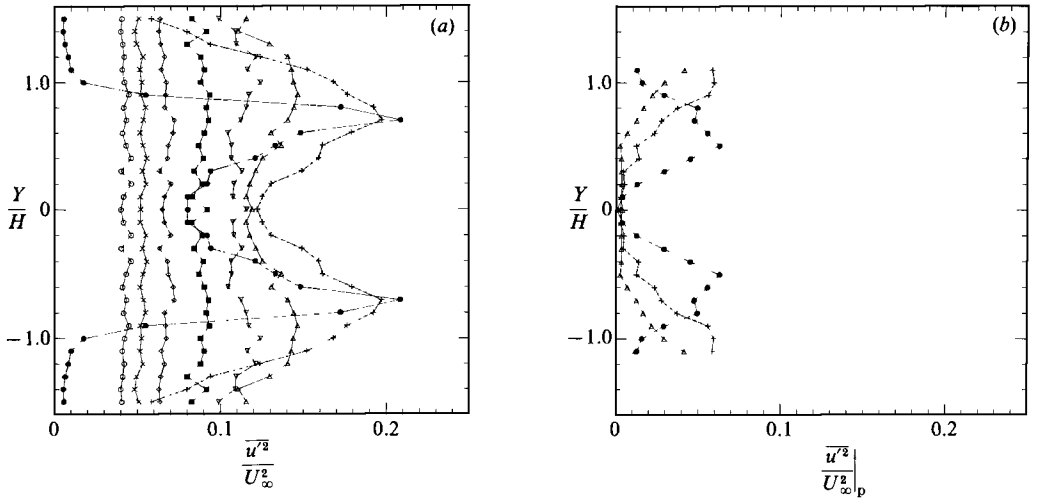

FIGURE 6. Streamwise normal stress obtained from (*a*) global data, (*b*) phase-averaged data (suffix p). Same case as figure 5. ●, $X/H = 1$; +, 3; △, 5; ▽, 7; ■, 9; ◇, 11; ×, 13; ○, 15.

bluff body. It can be seen that these vectors indicate reversed flow. Further downstream, say at $X/H = 10$ where H is the body height, these vectors occupy a cone which has an angle greater than the included angle of the wires. This leads to rectification problems even though the flow is not reversing. The obvious benefits of flying the wires are two-fold – first, rectification is eliminated and, secondly, the performance of the calibration scheme used here is improved as the cone angle is reduced.

Because of the high turbulence intensity in the wake of nominally two-dimensional bodies even as far downstream as $X/H = 15$ it is necessary to 'fly' the probe in order to gather meaningful measurements. Using a triple decomposition scheme, as used for example by Cantwell & Coles (1983), any flow quantity may be considered to

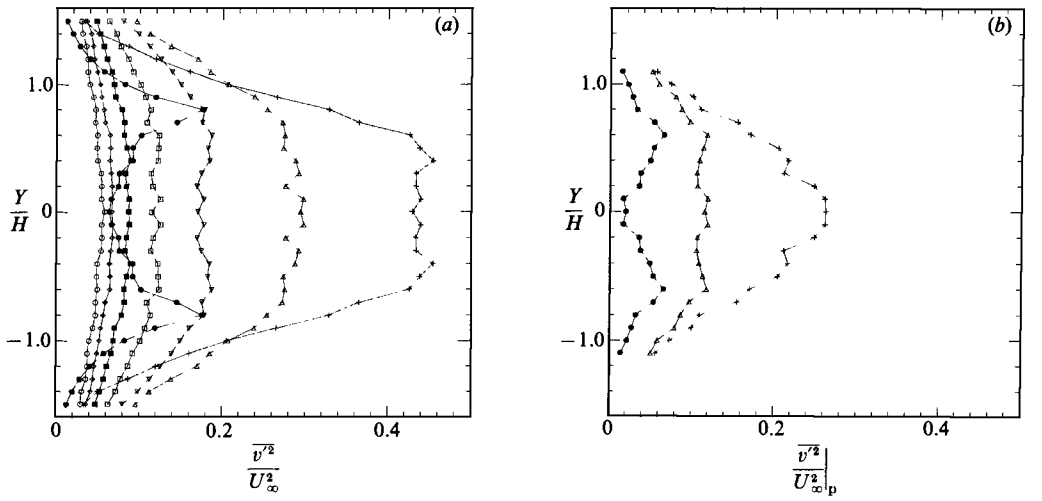

FIGURE 7. Cross-stream normal stress obtained from (*a*) global data, (*b*) phase-averaged data (suffix p). Same case as figure 5. Symbols as figure 6.

consist of a mean component, a periodic or phase-averaged component, and a truly random component. The mean and phase-averaged components may be estimated from the phase-averaged velocity data. Since the contribution of the random motions has been averaged out to get these data, it is necessary to run a separate experiment to measure the global stresses. Global stresses contain the contributions from both the periodic and random motions.

One way of doing this is to sample at given locations in the flow, once for each forward pass of the probe. Because a very high population of data samples is required for obtaining convergence of global stresses this direct approach would take an impracticably long time. However, a good approximation to this is to sample many times within a small length (say 100 samples each spaced 1 mm apart) centred about the required locations in the flow. In this way a large sample population may be built up in reasonable time (say 80000 samples in 40 min around each of 8 separate measuring stations). This was done for only the case of a normal bluff body with no end-plates attached. The results are presented in figures 5(*a*)–8(*a*), alongside the estimates obtained from the phase-averaged data (figures 5*b*–8*b*).

It is perhaps unexpected that the two sets of mean velocity profiles in figure 5(*a*,*b*) do not agree well even as far downstream as five body heights. This is because the phase-averaged data were obtained with the probe moving upstream at about $1.2U_\infty$ (U_∞ is the free-stream velocity measured about 1 m upstream of the bodies), whereas for the acquisition of global data the bias velocity of the probe was only about $0.75U_\infty$ (see figure 4*b*). The discrepancy shows that in order to correctly infer even mean flow velocities it is necessary to fly the wires very quickly through the flow. Unfortunately, this lesson was learned too late for the experiment to be repeated and so we do not have accurate estimates of global flow parameters. Nevertheless, it is believed that the effects of rectification were sufficiently reduced so that we can obtain approximate ratios of the phase-averaged stresses to the corresponding global stresses.

From figures 6(*a*, *b*) about 20 %–24 % of the global streamwise turbulent stress u'^2 is carried by the large-scale periodic motions. In comparison, Cantwell's (1976)

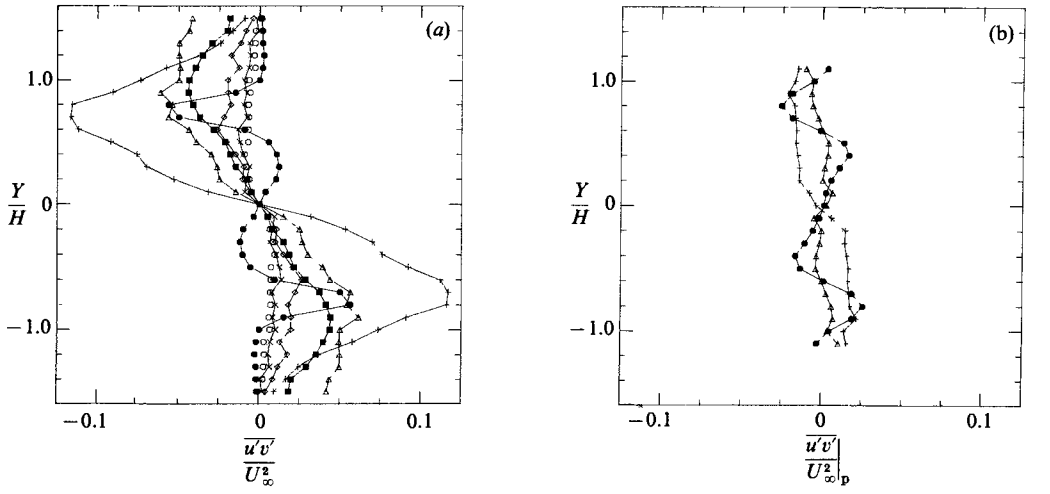

FIGURE 8. Shear stress obtained from (*a*) global data, (*b*) phase-averaged data. Same case as figure 5. Symbols as figure 6.

results for the turbulent wake behind a circular cylinder gave this proportion as 29 % at about the same relative position in the flow. Figures 7(*a–b*) show that the proportion of the global cross-stream turbulent stress $\overline{v'^2}$ attributable to the phase-averaged motions is about 50 %. Cantwell reported a comparable value of 40 % for this stress. Profiles of Reynolds shear stress $\overline{u'v'}$ are given in figures 8(*a*, *b*). The phase-averaged motions appear to contribute only about 10 % to the global value of this parameter, compared to Cantwell's value of 36 %. The reason for this comparatively large disagreement is not known.

The efficacy of the flying-hot-wire system in the measurement of Reynolds shear stress has been recently tested in wall turbulence. An agreement between stationary wires and flying wires was obtained for cases where the spread in vector directions was not too large.

4.3. *Elliptical planform at an angle of attack*

Work by Lim (1979) and Perry & Tan (1984) showed that buoyancy could lead to the inhibition of shear-layer roll-up on one side of a coflowing free-shear flow. In those experiments, an 'inner' flow was issued from a tube into the surrounding free-stream or 'outer' flow. The tube was aligned with the outer flow. The fluid for the inner and outer flows came from different sources so that the properties of the fluids could be varied independently of one another.

In this type of configuration, a density difference between the inner and outer flows leads to the formation of trailing vortices in the mean. Single-sided structures, as shown in figure 1(*b*), are seen in this flow. Similar experiments by Anderson (1981) in a vertical wind tunnel revealed that single-sided structures would also be produced when trailing vortices were introduced by a deliberate misalignment of the tube in the outer flow.

Following on from this work, preliminary observations in a flow-visualization wind tunnel indicated that a three-dimensional body, which produces lift and therefore develops trailing vortices, could also have a single-sided wake. It appears that the single-sided nature of such a wake must be associated with the system of trailing

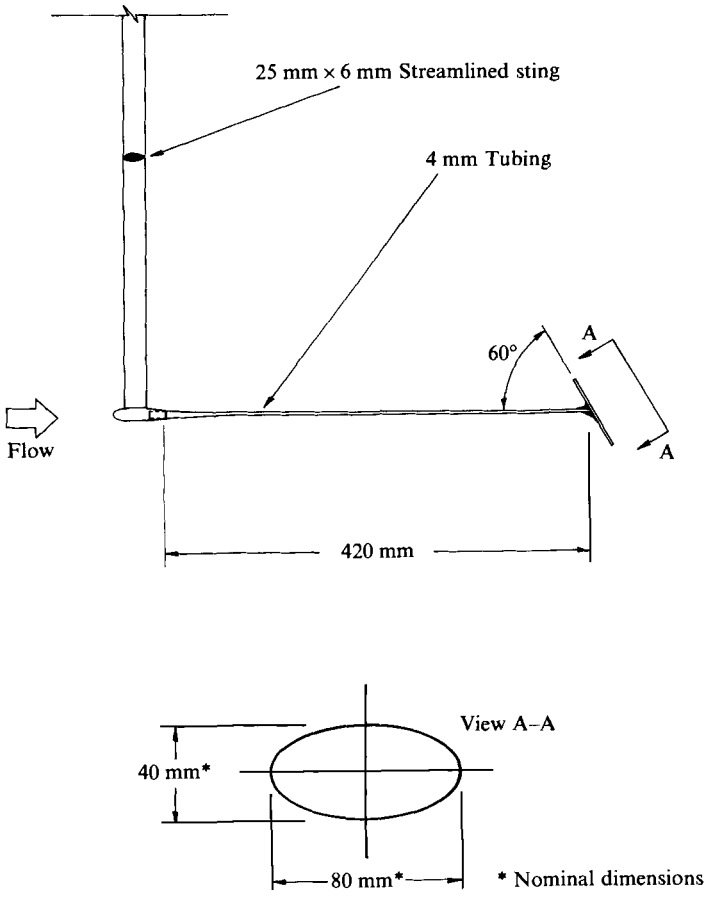

FIGURE 9. Elliptical planform and support.

vortices. One body which appeared to exhibit this behaviour quite clearly was a flat plate in the shape of an ellipse, placed at an angle of attack. The model used, and the associated support apparatus, are shown in figure 9.

Calvert (1967) examined the flow behind a circular disk at an angle of attack of about 50°. From the results of flow visualization, he described the wake as consisting of vortex loops shed from the trailing edge of the disk. In photographs that he provides it does seem that vortices roll-up only on the trailing edge side of the wake. A closer examination however, shows that it may be possible that Calvert merely failed to make visible eddies that exist on the leading edge side of the wake. It does appear however that if they exist at all, these must be weaker than the eddies on the trailing edge side of the wake, judging by the relatively small deflection of the smoke streaklines on the leading edge side of the wake.

Phase-averaged velocity-vector fields and integrated streamline patterns for the nominal plane of symmetry of the wake behind the elliptical planform at an angle of attack, are presented in figures 10(*a*)–(*h*). In this flow the major axis of the ellipse was aligned with the spanwise direction. These eight plots represent the flow field over one half of the vortex shedding cycle. They are viewed by an observer moving with the pattern at a velocity of 3.6 m/s downstream and 0.36 m/s vertically downwards. The downstream component of the convection velocity of the pattern

was determined by the technique described in §3. The value of the cross-stream component of convection velocity relative to the streamwise component was chosen to be consistent with the translation of eddying motions over one cycle as seen in the vector fields. The vectors closest to the body were measured at a station $X/C = 3.75$ behind the centre of the body, where C is the length of the minor axis of the ellipse.

The wake in these figures appears as a repeated pattern of pairs of counter-rotating vortices. There is a 'mushroom'-like appearance which is conjectured to be a consequence of the measuring plane cutting through a series of vortex ring like structures. This looks like the simple smoke-pattern structure shown in figure 1 (*c*).

Following the development of the clockwise-rotating eddy at the left-hand side of figures 10 (*a*)–(*h*), we see that the motion at first shows a strongly unstable focal behaviour. This is indicative of a vortex filament lying normal to the measuring plane and being subjected to significant compressive axial strain rate. The strength of this strain rate is reduced over the next two phase intervals (figures 10*b*, *c*) as the eddy appears increasingly more focal, that is phase-averaged streamlines wrap around the critical point for a greater number of rotations. The eddy at this stage still appears as an unstable focus. Over successive phase intervals this eddy changes topologically, appearing as an unstable limit-cycle pattern and then later as an increasingly stable focus.

These integrated streamline patterns by no means contradict the flow-visualization results of the authors, or those of Calvert. It is conjectured that the near-wake region consists of structures similar to vortex rings, except that the vorticity on the upstream side of each ring has been 'smeared out'. This is shown in figure 11. Although the vorticity varies around the ring, the circulation is constant. Such a ring leads to single-sided 'loop'-like flow structures as shown in figure 1 (*a*).

In the case of loop-like structures, the smeared-out regions of relatively low-vorticity shear-layer material will not roll-up as tightly as the more concentrated regions of vorticity and so do not appear as eddy-like. It is not surprising that flow visualization fails to distinguish such smeared-out regions of relatively low vorticity since stronger eddying motions are shown up more clearly than weaker ones. Flow visualization with smoke also shows up stable foci which 'concentrate' the smoke far more clearly than unstable foci which 'dissipate' the smoke. It is possible that Calvert's flow visualization showed this flow to consist of vortex loops for these reasons. However, the streamline patterns can be explained and reconciled with the flow-visualization results of Calvert. Since the body is three-dimensional and is producing lift, isolated trailing vortices must exist. These trailing vortices induce a lateral compressive straining in the plane of symmetry above themselves, and a stretching below. There also exists a downwash between the two trailing vortices. All this is consistent with the movement and change in type of critical point that is observed in the integrated streamline patterns, and also with the flow-visualization results reported by Calvert. After the eddying motion on the leading-edge side of the wake (in this sectional view) moves below the level of the trailing vortices under the effect of the induced downwash, it experiences stretching. This has the effect of increasing the vorticity of the smeared-out side of the ring and so the eddy appears increasingly focal with streamwise distance. The lower part of the ring has been continually stretched while the upper part has first been compressed and then later stretched. This accounts for the fact that the upper part appears consistently weaker in vorticity than the lower one in this section of the flow. This is evident in figure 12 which shows contours of phase-averaged vorticity at one phase of the flow cycle.

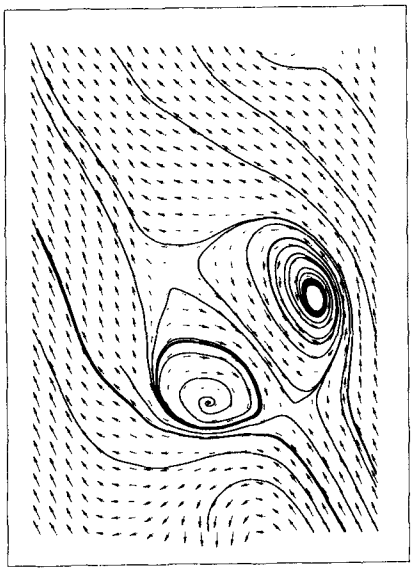

(e)

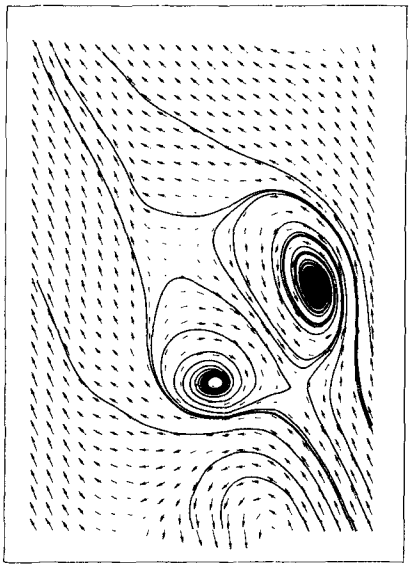

(f)

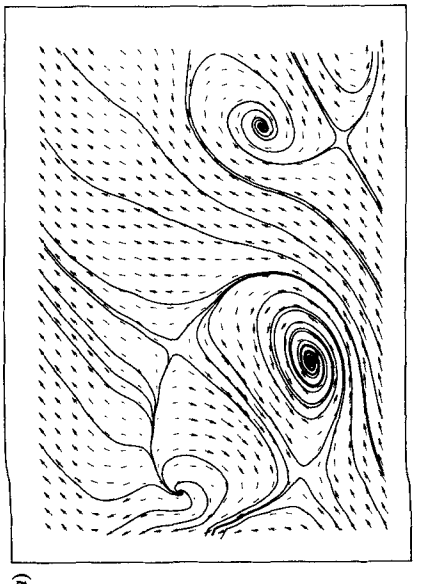

(a)

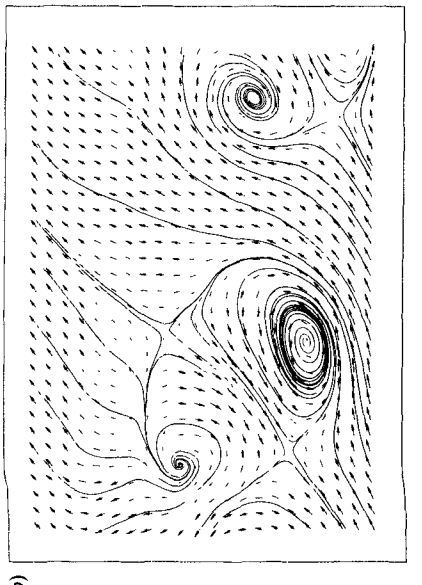

(b)

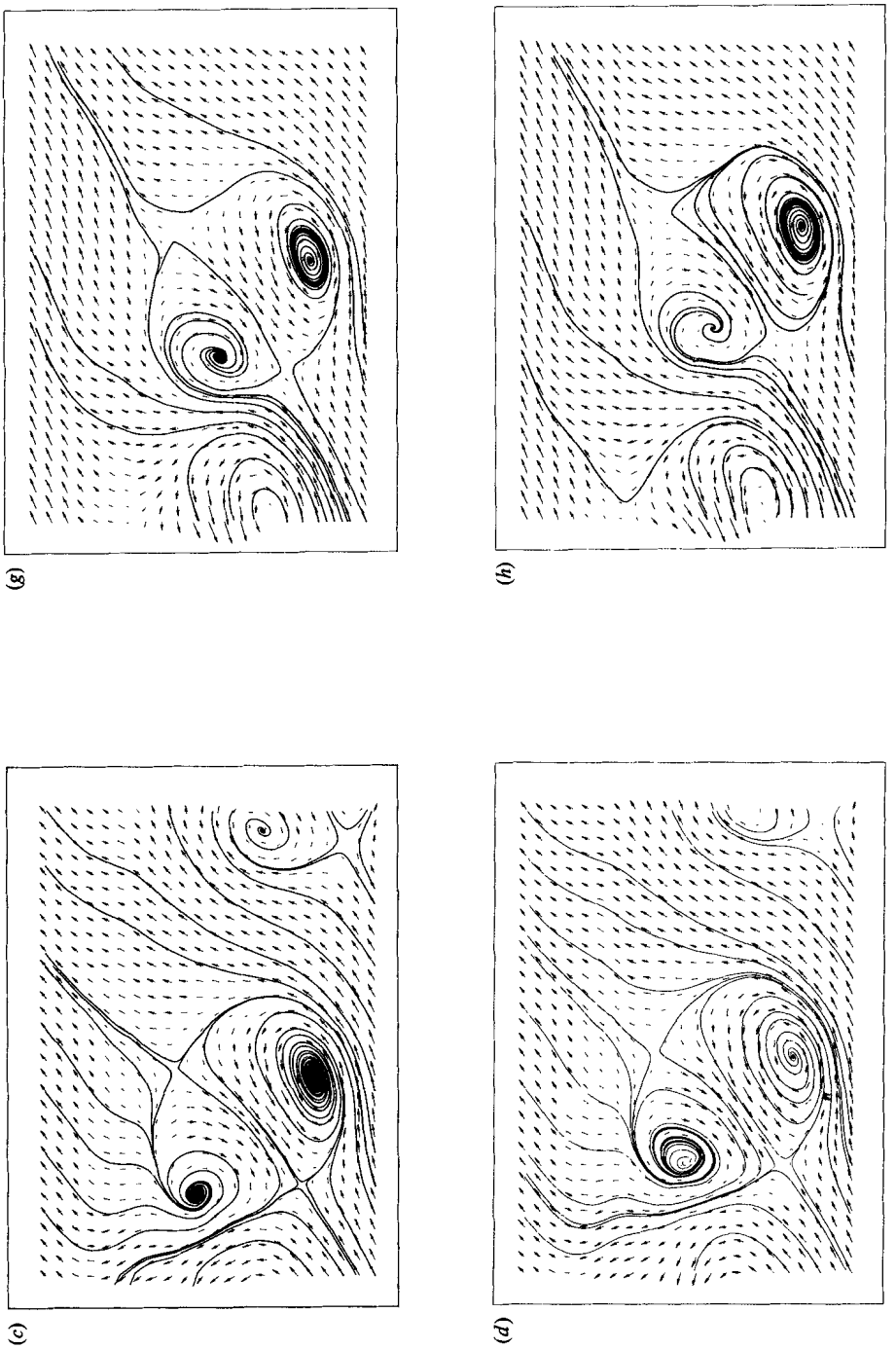

FIGURE 10. Phase-averaged velocity-vector fields and integrated streamline patterns behind elliptical planform at an angle of attack. Observer moving downstream with the pattern at 3.6 m/s and vertically downwards at 0.36 m/s. (*a*)–(*h*) correspond respectively to phases 1–8.

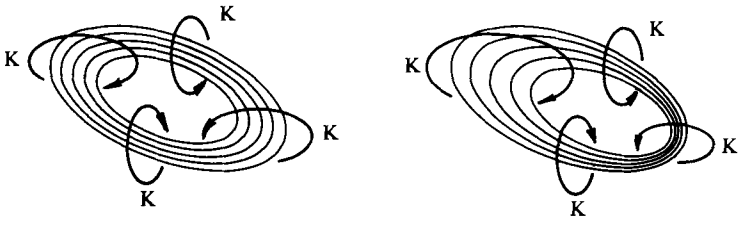

FIGURE 11. Vortex-ring-like structures. In both cases the circulation K is constant around the ring, but in the case of (*b*) vorticity varies in the circumferential direction. Structures like (*a*) lead to the appearance of mushrooms and structures like (*b*) lead to the appearance of loops.

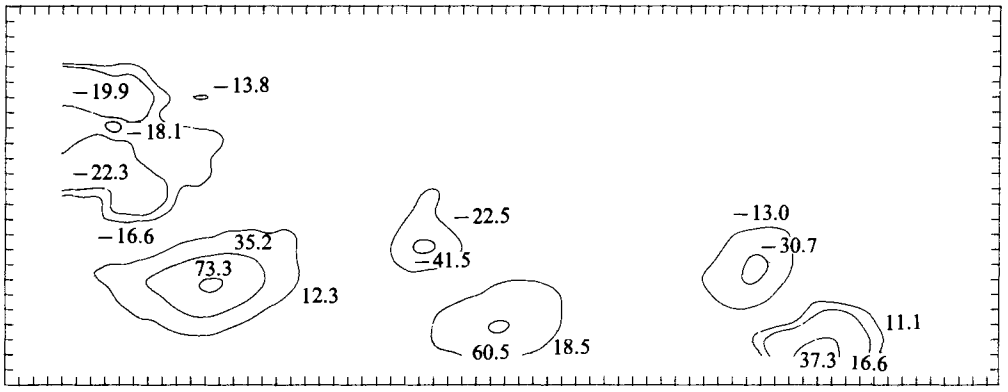

FIGURE 12. Contours of phase-averaged non-dimensionalized vorticity $\omega h/U_\infty$ for phase 1 of the vortex-shedding cycle of the flow behind the elliptical planform at an angle of attack. The left-hand half of this plot corresponds to figure 10(*a*). (ω is the component of vorticity in the measuring plane, and U_∞ is the free-stream velocity; h is the chord length of the elliptical planform.)

4.4. *Flapping flag*

The wake behind a flapping flag is an extremely periodic three-dimensional flow and so it is a case well suited to the techniques of phase averaging. The suitability of various flags was tested by observing their motion under stroboscopic lighting. Flags having a tendency to twist or behave asymmetrically were rejected. The flag eventually used for the experiments was made of a lightweight woven synthetic cloth in the shape of an isosceles triangle. The flag and its support apparatus are sketched in figure 13.

One half of the velocity vector field in the nominal plane of symmetry is shown for a typical phase of motion in figure 14. The field extends in the cross-stream direction from the wake centreline to about $Y/L = 2.25$, where L is the length of the flag (67 mm). The measurements shown are for streamwise stations between $X/L = 6.75$ and $X/L = 16.5$. The observer's frame of reference is translating downstream at 3.6 m/s and away from the centreline at 0.125 m/s. This cross-stream translational velocity is necessary since the flag wake is spreading and the observer must move with the eddies if they are to be correctly interpreted. The relative magnitudes of the convection velocity components were chosen to be consistent with the translation of eddies, seen in the vector fields, through one cycle of the motion as was done for the preceding elliptical planform case.

The wake shows up as a series of regions of relatively strong 'upwash' bursts, each

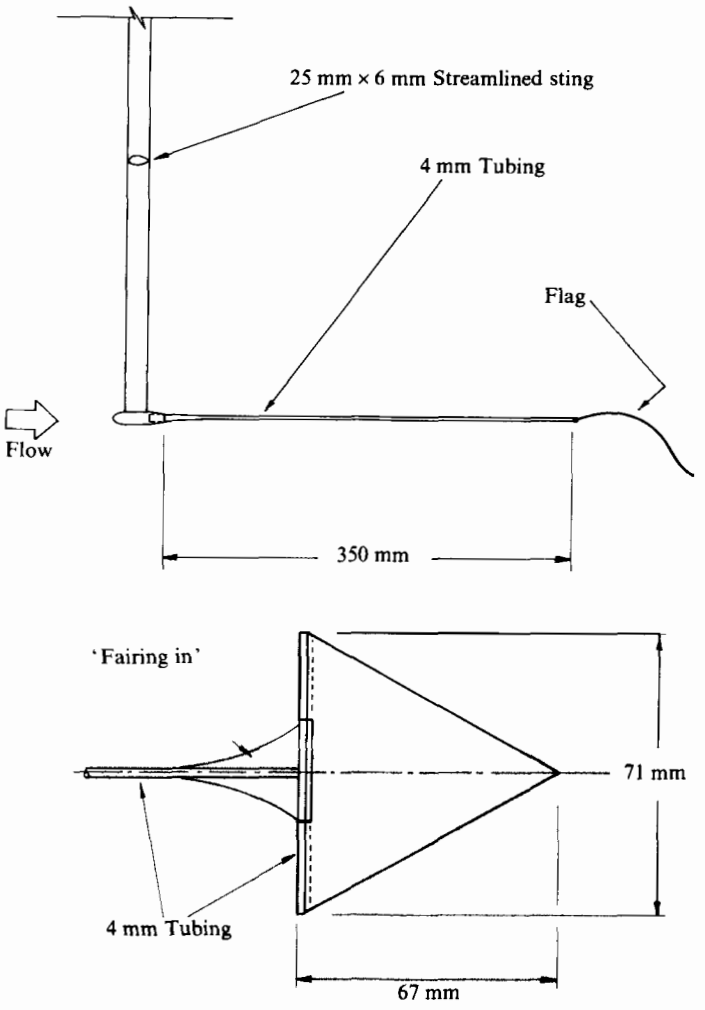

FIGURE 13. Flag and flag support.

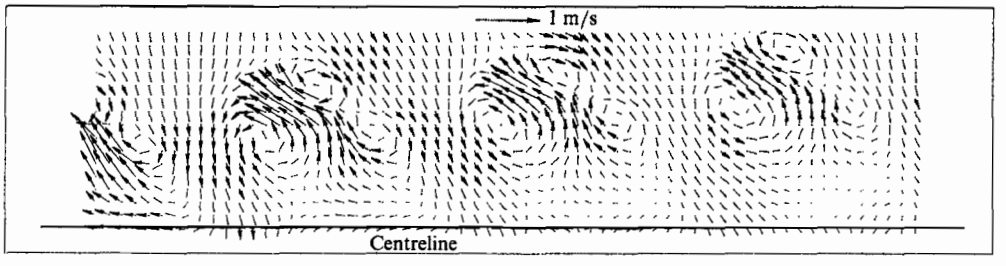

FIGURE 14. Far-wake velocities (half-field) behind flapping flag as seen by an observer moving downstream at 3.6 m/s and away from the wake centreline at 0.125 m/s.

of which leans upstream away from the centreline of the wake. There is one eddying motion visible on the upstream side of each burst, and two are visible on the downstream side. The two eddies on the downstream side share the same sign of vorticity, and the eddy on the upstream side has the opposite sign of vorticity.

The integrated sectional streamline pattern for the upstream half of figure 14 is

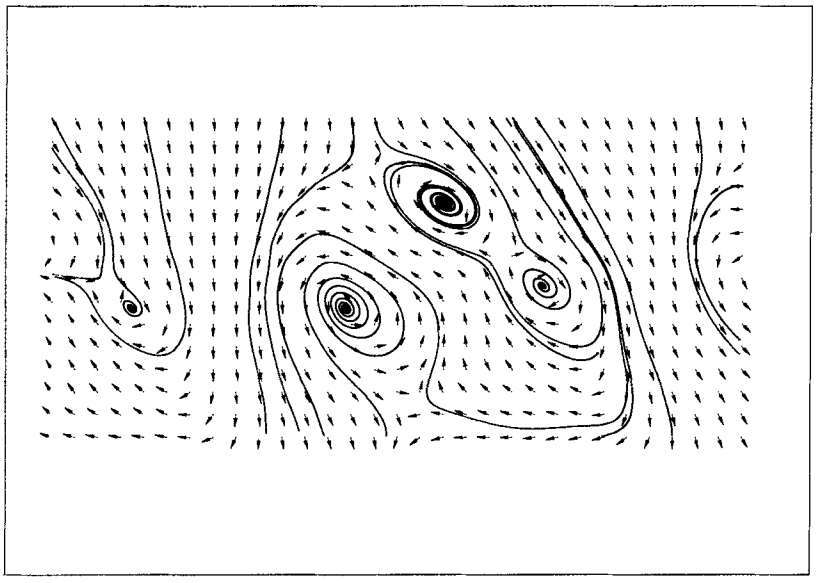

FIGURE 15. Velocity field and integrated streamline pattern corresponding to the left-hand (upstream) half of figure 14.

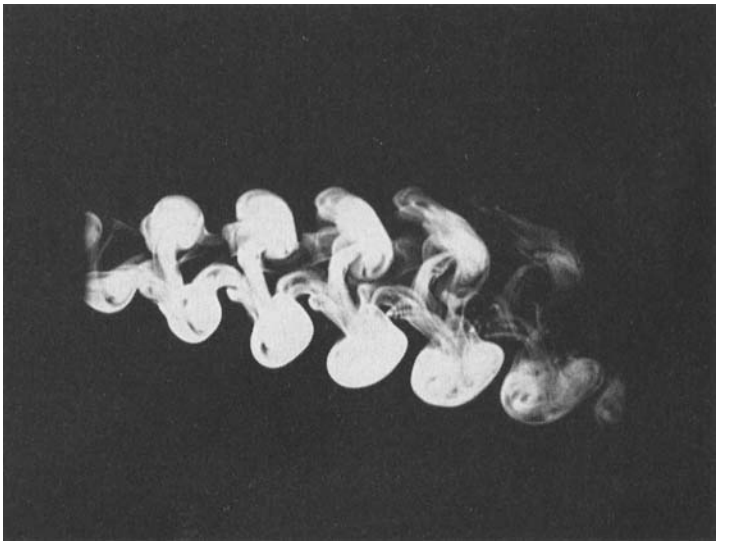

FIGURE 16. Negatively buoyant coflowing jet. Note the appearance of mushroom structures on the lower side of the flow. Flow is from left to right. Reynolds number here is of the order of 1000 based on tube outlet diameter.

shown in figure 15. It appears that the eddies on the downstream side of the upwash bursts form stable foci, while the eddy on the upstream side forms an unstable focus. A coflowing 'mushroom' structure has been produced similar to those studied by Lim (1979), and Perry & Tan (1984). This is included for comparison with the flag wake and is shown in figure 16. This flow is actually a jet and the mushrooms are pointing downstream, whereas in the flag-wake results presented here the mushrooms point

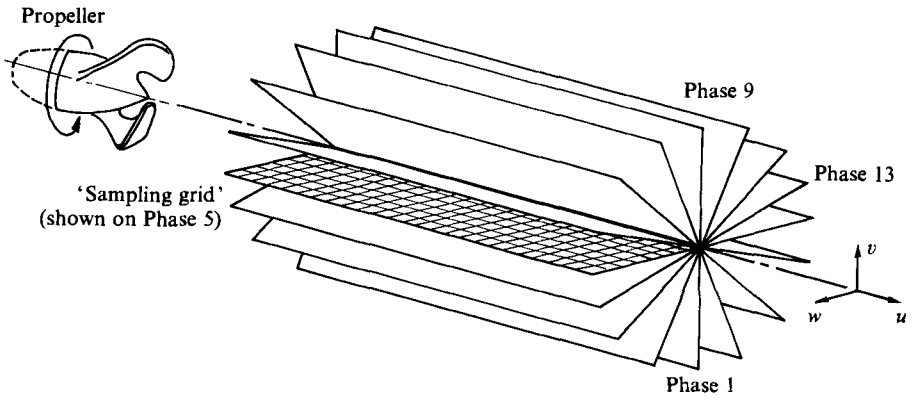

FIGURE 17. Phases of the vortex-shedding cycle shown as rotating 'sheets' with velocity vectors attached at points on a sampling grid. Velocity components u and v lie in the measuring plane.

upstream. The flow appears to be a slightly more complex version of the structure in figure 1 (*d*).

To understand how the combination of two eddies is formed on the downstream side of the upwash bursts it is necessary to examine the movement of the flag. The motion of the flag consisted of a general and fairly gentle waving over most of the flag, followed by a strong 'flick' of the tail at the end of each stroke. It is possible that some feature of this motion leads to an apparent splitting of the vortex ring around the upwash bursts. It may also be possible that two similar vortex rings are formed close to each other in such a way that their upstream sides wrap around each other and effectively 'pair'. The downstream sides may be prevented from such a pairing, or else the process may take longer to occur. This may be similar to an imperfectly executed 'leap-frogging' of two vortex rings.

4.5. *Propeller wake*

Owing to the special symmetry properties of the flow behind a propeller, we have a unique opportunity to produce a complete three-dimensional flow field with the minimum of data gathering, by simply measuring in one plane. Furthermore, this flow case enables us to examine the topological properties of the flow patterns around stretched vortices that cut the measuring plane obliquely. It will be seen that this kind of configuration leads to the appearance of a rather unusual limit-cycle pattern.

An observer rotating with the propeller, but not translating relative to it, would 'see' a steady pattern. Such an observer would detect a 'fixed' three-dimensional velocity field. A stationary observer, however, would see a velocity field that varies cyclically. This velocity field could be represented by a set of velocity vectors attached to a grid that rotates with the propeller. Such an arrangement is sketched in figure 17. Sixteen 'sheets' are arranged radially, intersecting along the axis of rotation of the propeller and the wake. Each sheet contains the three phase-averaged velocity components at one phase for points distributed in a single streamwise measuring plane.

Since the cross-wire probe is capable of resolving only two components of velocity at one time, it was necessary to run the propeller experiment twice, rotating the probe through 90° between experiments, in order to measure three orthogonal velocity components. The wind-tunnel and propeller speeds were carefully set to be the same

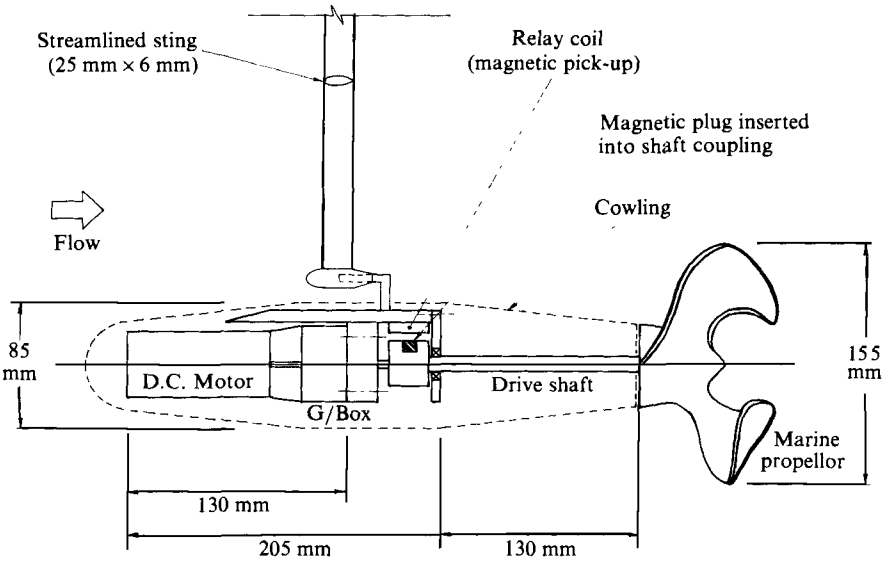

FIGURE 18. Details of propeller drive unit and support.

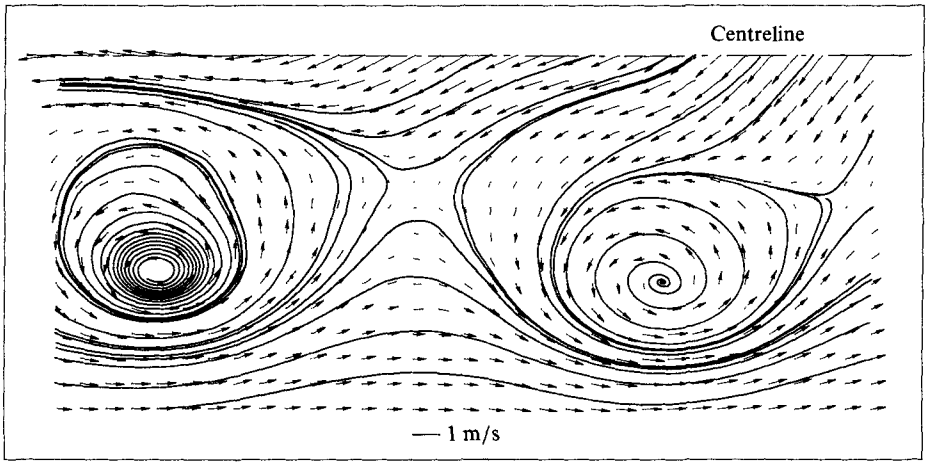

FIGURE 19. Streamwise sectional velocity field and integrated streamline pattern at a typical phase of motion in the far wake behind the propeller. Observer moving downstream at 3 m/s.

for the two experiments, and the redundant set of axial velocity measurements allowed a check for the accuracy of 'matching' of the two data sets. No correction to the velocity was needed.

The flow was generated by rotating a propeller in a surrounding free-stream flow such that a wake was produced. That is the propeller was operated as a windmill. This mode of operation was chosen after flow visualization indicated that it produced a more clearly defined pattern downstream of the propeller.

The two-bladed marine propeller used gave the best results out of several types that were tested. The entire apparatus, which resembled a torpedo with the propeller at the rear end, was hung from an airfoil section sting. The unit is shown in figure 18.

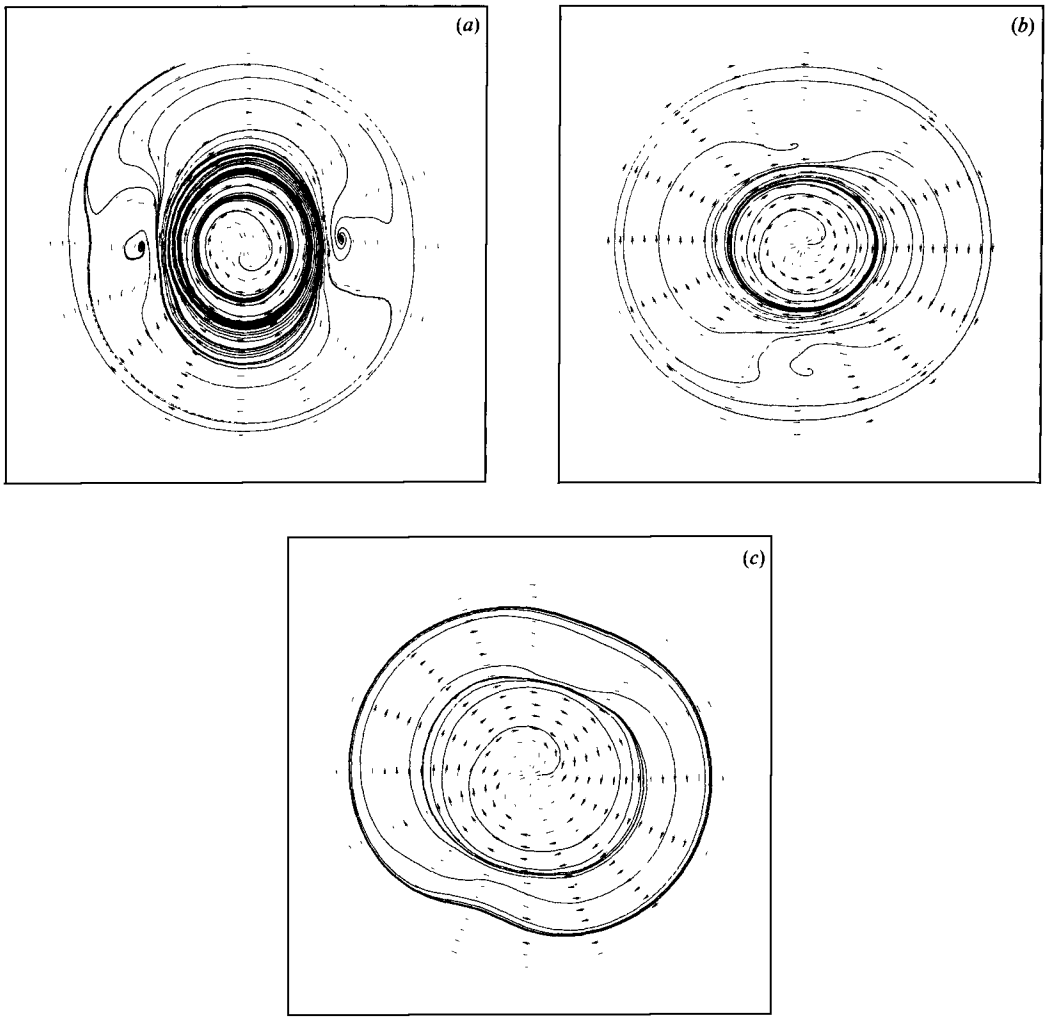

FIGURE 20. Cross-sectional velocity field and integrated streamline pattern at (*a*) $X/D = 4.5$; (*b*) 5.2; (*c*) 7.5 (D = propeller diameter).

Phase detection was achieved by using a magnetic pick-up to detect the rotation of the propeller drive shaft. A magnetic plug was inserted into the coupling joining the propeller shaft to the output spindle of the gearbox. The rotation of the plug was detected by a small stationary wire coil. Originally a normal hot-wire was used to provide the basis for phase sorting. Despite the periodicity of the flow a small degree of 'wafting' of the wake led to a noticeable washout of the velocity vector field. The magnetic pick-up allowed perfect phase detection and this led to a faster convergence of the measured data. There was the additional advantage that the phase detection was identical in the two experiments when different velocity components were being measured on separate occasions.

The velocity field and integrated phase-averaged streamline pattern for a streamwise sectional plane at a typical phase of the propeller rotation is given in figure 19. For reasons that will be made clear in §5, it is important to remember that for this case the measuring plane is not a nominal plane of symmetry and so we are forced

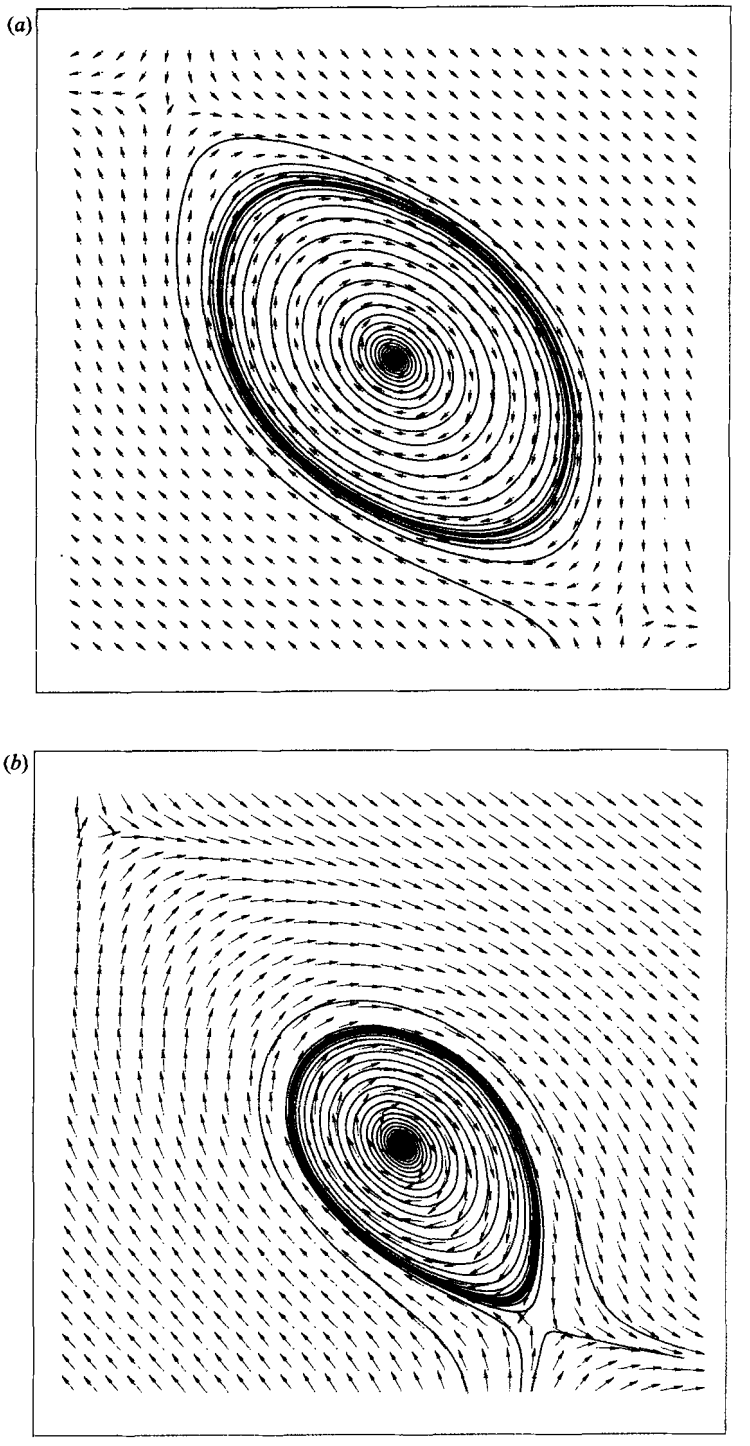

FIGURE 21. (*a*) Sectional velocity field and integrated streamline pattern around a Burgers' vortex cut by a sectioning plane through the origin at $z = 0$ (see equation (A 2)). The planes intersect at 60°. (*b*) The sectioning plane now intersects the vortex away from the origin at $z = 0$.

to interpret the flow via sectional streamline patterns as described in Part 1, §1. The pattern here is observed in a non-rotating frame of reference moving horizontally downstream at 3 m/s without any cross-stream component. The two eddies shown appear as rather unusual limit-cycle patterns. They both appear unstable in the small but it is difficult to tell if they are stable or unstable in the large. Altering the velocity of the observer relative to the flow field does not change the odd appearance of the pattern significantly although the critical points do shift slightly. More will be said on the appearance of these patterns in the next section.

The vector fields and the integrated streamline patterns revealed by cross-stream sectional cuts of the wake are presented in figures 20(*a–c*). These results show measurements from streamwise stations at $X/D = 4.5$, 5.2 and 7.75 respectively, where D is the propeller diameter. These patterns are as seen by a stationary (non-rotating) observer looking upstream.

The first pattern in this sequence shows three eddying motions. The outer two foci are cross-sectional views of the propeller-tip vortices. Closer to the centre of the wake there appears to be an unstable limit cycle. Inside this there appears to be a neutrally stable limit cycle which instantaneous streamlines approach from the outside and leave on the inside. At the very centre there appears to be another focus. This swirling motion seen over the central region of the wake is due to the propeller-blade root vortices which are trailing downstream and are of like sign so that even after they merge there exists a net vorticity in this core region. All three foci are stable. This is reasonable since the velocity defect in the wake is weakening with streamwise distance and so there exists streamwise acceleration and a positive streamwise strain rate. The spiralling in of instantaneous streamlines is consistent with the existence of a strain rate of this sign.

The phase-averaged tip vortices appear weak five propeller diameters downstream and almost indiscernable by eight diameters downstream. This is probably due to diffusion of vorticity since, in the case of a propeller rotating at constant speed in a steady free-stream, the degree of phase jitter should be small.

5. The appearance of limit cycles in strained vortex flows viewed in oblique sectioning planes

Imagine we are viewing the flow surrounding a vortex being stretched along its axis, in a sectioning plane normal to the vortex. The flow pattern in such a case always shows up as a focus. Some co-workers have suggested privately that the appearance of limit cycles in such a sectioning plane is an illusion caused by the plane being slightly non-orthogonal to the stretching direction, rather than being indicative of true multiple-celled behaviour as exemplified by the two-celled 'Sullivan' vortex (see Sullivan 1959 and Part 1, §4). This idea has been tested here using the simple Burgers' vortex (see Burgers 1948) which models a viscous vortex rod subjected to axisymmetric strain rate aligned with the vortex rod. This flow is defined by (A 1) in the Appendix. A steady-state solution exists for this vortex flow and this has a Gaussian distribution of vorticity with radius. This flow appears as a focus with radial symmetry in the plane orthogonal to the stretching axis (see Part 1, figure 29*a*). It is found that limit cycles appear in the sectioning plane only when the normal to that plane intersects the straining axis at an angle greater than about 55°. As a matter of interest, a variety of patterns may be obtained by sectioning a Burgers' vortex and a topological classification can be made based on two parameters. Details of this are provided in the Appendix.

Limit cycles seen in sectioning planes which cut a Burgers' vortex at a large angle in the way just described have an unusual appearance as shown in figure 21 (*a*), which is the view in a sectioning plane which cuts the vortex obliquely through the origin at $z = 0$. In figure 21 (*b*) a pattern for a sectioning plane which intersects the vortex away from the plane of symmetry is shown and this bears a resemblance to the experimental propeller-tip vortex patterns seen in the streamwise measuring plane in figure 19. These propeller-tip vortices appear as limit cycles in a measuring plane which they cut at an angle of about 57°. As previously mentioned these tip vortices appear as stable foci when viewed in a cross-stream sectioning plane. The axes of the vortices make an angle of about 33° to the normal of these planes. This change in the type of flow pattern with the angle of the sectioning plane is in agreement with the analysis and findings presented in the Appendix, which is believed to have some relevance here as an approximation to the flow around the propeller-tip vortices. It is possible then that these limit cycles are not of the Sullivan-vortex type. However, on the basis of this investigation, the authors contend that limit cycles observed in the other cases presented here are due to genuine multiple-celled behaviour since measurements were then taken in a plane of symmetry.

6. Conclusions and discussion

Turbulent wakes behind a variety of vortex-shedding bodies have been examined using a phase-averaging technique in conjunction with a flying-hot-wire system. It has been found that even as far as 15 body lengthscales downstream it is necessary to impose a significant bias velocity on the hot-wire probe so as to alleviate problems associated with large variations in velocity-vector direction.

Various topological features of the large-scale eddying motions downstream of the vortex formation region have been identified. The basic classification scheme shown in figure 1 was in part derived from earlier work on periodic laminar-flow coflowing jets and wakes, and this appears to fit in well with the observed phase-averaged motions in turbulent flows presented here.

A nominally two-dimensional plate, placed normal to the flow and also at an angle of attack, produces double-sided 'loop'-like structures. In the nominal plane of symmetry these flows resemble the classical Kármán vortex street, except that the flow is three-dimensional as evidenced by the appearance of foci and limit cycles. It is conjectured that this is associated with a spanwise waviness in the shed vortices.

As shown from previous work, a three-dimensional body at zero angle of attack such as an ellipsoidal body with its major axis aligned in the spanwise direction also produces a wake with a double-sided structure and the vortices are shed in a plane normal to the major axis. However, it is shown that an elliptical plate placed at an angle of attack has a wake consisting of single-sided 'mushroom'-like structures. On the basis of Calvert's results it is possible that close to the body the wake consists of single-sided 'loop'-like structures, although this has yet to be verified. The lack of symmetry in the wakes behind three-dimensional lift-producing bodies appears to be caused by the trailing vortices.

The flapping flag produced a wake with double-sided 'mushroom'-like structures which resemble the coflowing jets produced by Perry & Tan (1984). The flow behind the propeller represents one of the few cases where an entire three-dimensional phase-averaged velocity field can be mapped out by taking measurements in only one plane. In addition it enables sectional streamline patterns to be obtained around vortices where the vorticity vector cuts the measuring plane obliquely. The angle of intersection may be controlled by a simple adjustment of the flow parameters.

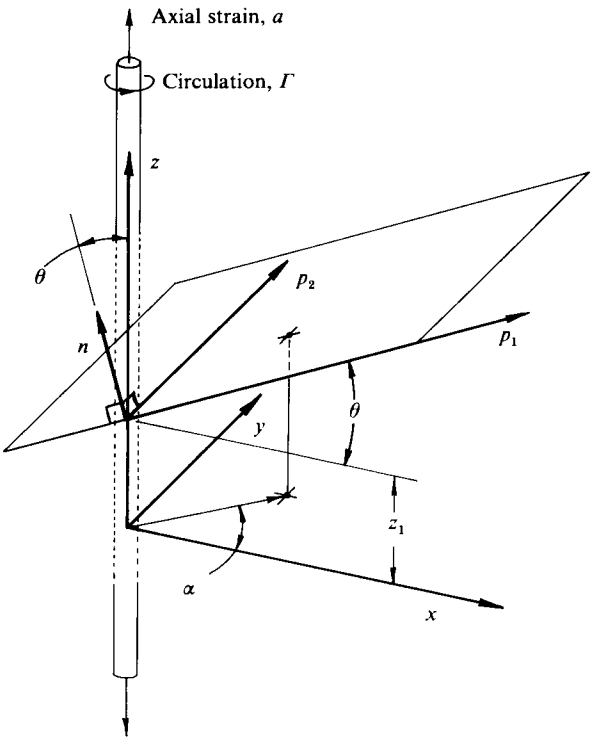

FIGURE 22. Configuration and notation for the analysis of a Burgers' vortex velocity field being resolved onto an arbitrary sectioning plane.

The role that these large-scale motions play in the turbulent transport processes behind bluff bodies needs to be resolved. They are certainly visible in flow-visualization experiments although the superimposed fine-scale motions cause a loss of definition of the smoke structures. Although the large-scale phase-averaged motions contribute significantly to the Reynolds normal and shear stresses, most of the contributions are attributable to the finer-scale motions. It should be kept in mind however, that phase jitter leads to a weakening of the measured phase-averaged contributions and so the actual contributions may be greater than indicated by the measurements here. These large-scale motions probably play an important role in the transport and stretching of the finer-scale motions and so cannot be ignored in any turbulence modelling that is aimed at producing physically realistic results.

Appendix

Let us consider the configuration shown in figure 22. A vortex rod is aligned with the z-axis. An arbitrary cutting plane intersects the z-axis at $z = z_1$, and the normal defining the plane makes an angle θ with the z-axis. Without loss of generality the coordinates in the plane (p_1, p_2) are defined such that the p_1- and x-axes intersect at an angle of θ, and the p_2- and y-axes are parallel. The (p_1, p_2)-origin lies at $(x, y, z) = (0, 0, z_1)$. The Burgers'-vortex solution is

$$u_r = -ar, \quad u_\theta = \frac{\Gamma}{2\pi r}\left[1 - \exp\left(\frac{-ar^2}{2\nu}\right)\right], \quad u_z = 2az, \tag{A 1}$$

where a is the axial strain rate, Γ is the circulation around the vortex rod, ν is the kinematic viscosity, and (r, θ, z) are the radial, circumferential and axial coordinates respectively.

From this it may be shown that

$$\left.\begin{aligned} \dot{p}_1 &= ap_1(3\sin^2\theta - 1) - \frac{\Gamma p_2 \cos\theta}{2\pi r^2}\left[1 - \exp\left(\frac{-ar^2}{2\nu}\right)\right] + 2az_1 \sin\theta, \\ \dot{p}_2 &= \frac{\Gamma p_1 \cos\theta}{2\pi r^2}\left[1 - \exp\left(\frac{-ar^2}{2\nu}\right)\right] - ap_2, \end{aligned}\right\} \tag{A 2}$$

where $$r^2 = x^2 + y^2 = p_1^2 \cos^2\theta + p_2^2.$$

Having a non-zero value of z_1 only has the effect of adding a uniform flow component parallel to the p_1-axis in the (p_1, p_2)-plane. We shall for the moment consider the case where $z_1 = 0$. Using dimensional analysis it may be shown that

$$\dot{\boldsymbol{p}}^* = f\left(\boldsymbol{p}^*, \frac{\Gamma}{\nu}, \theta\right), \tag{A 3}$$

where * indicates lengthscales non-dimensionalized by (ν/a), $\boldsymbol{p}^*$ is the position vector in the (p_1, p_2)-plane non-dimensionalized by $(\nu/a)^{\frac{1}{2}}$, and $\dot{\boldsymbol{p}}^*$ is the velocity vector in the (p_1, p_2)-plane non-dimensionalized by $\Gamma/(\nu/a)^{\frac{1}{2}}$. This equation tells us that velocity is a vector function of the position vector and the two scalar parameters Γ/ν and θ.

If we have $ar^2/2\nu$ small and $z_1 = 0$, then to a linearized approximation

$$\left.\begin{aligned} \dot{p}_1 &= a(3\sin^2\theta - 1)p_1 - \frac{a\Gamma\cos\theta}{4\pi\nu}p_2, \\ \dot{p}_2 &= \frac{a\Gamma\cos\theta}{4\pi\nu}p_1 - p_2. \end{aligned}\right\} \tag{A 4}$$

Using phase-plane methods it can be shown that focal behaviour near to the critical point at the origin can only be seen in the (a_1, p_2)-plane when

$$\left(\frac{\Gamma}{\nu}\right)^2 > (4\pi)^2 \frac{3\sin^2\theta - 1}{\cos^2\theta} \tag{A 5}$$

and stable foci (with strain rate a positive) require

$$\theta < 54.74°. \tag{A 6}$$

Furthermore, nodal behaviour can only appear for

$$\left(\frac{\Gamma}{\nu}\right)^2 < (6\pi \tan\theta)^2. \tag{A 7}$$

It is possible to produce a 'map' of the behaviour of the flow in $[\theta - \log(\Gamma/\nu)]$ space, as seen in the (p_1, p_2)-plane. The map shown in figure 23 has boundaries defined by (A 5), (A 6) and (A 7). The map was verified by calculating the velocity field according to the unlinearized equations (A 4) and numerically integrating to determine streamline patterns for many different combinations of the scalar parameters $(\theta, \Gamma/\nu)$.

There exists a region on this map where limit-cycle-like behaviour is evident. For this to occur, however, it is necessary that the 'measuring plane' cuts the vortex filament at a large angle. When vortices are being cut obliquely care must be taken in the physical interpretation of limit cycles. The limit cycles generated in this

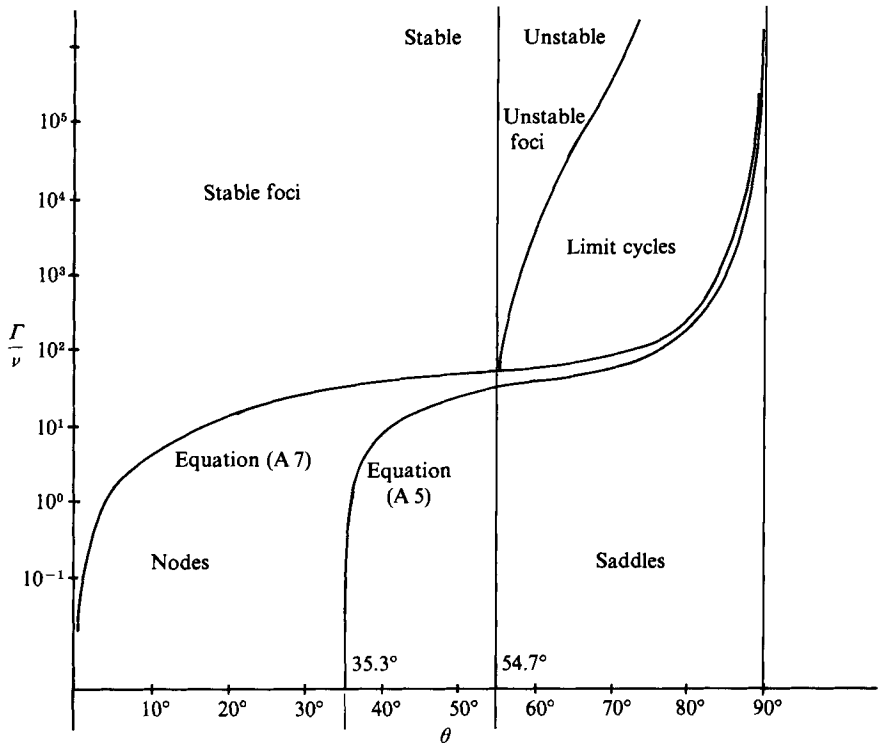

FIGURE 23. Map of the patterns observed in an arbitrary plane cutting through a Burgers'-vortex velocity field.

Appendix are not a result of true streamlines indicating multiple-celled behaviour but are indicated by sectional streamlines in oblique cutting planes with a sufficiently large value of θ.

REFERENCES

ANDERSON, J. M. 1981 The structure and dynamics of periodically stimulated jets and wakes. Ph.D. thesis, University of Melbourne.

BURGERS, J. M. 1948 A mathematical model illustrating the theory of turbulence. *Adv. Appl. Mech.* **1**, 171–199.

CALVERT, J. R. 1967 Experiments on the flow past an inclined disk. *J. Fluid Mech.* **29**, 691–703.

CANTWELL, B. J. 1976 A flying hot-wire study of the turbulent near wake of a circular cylinder at a Reynolds number of 140000. Ph.D. thesis, California Institute of Technology.

CANTWELL, B. J. & COLES, D. 1983 An experimental study of entrainment and transport in the turbulent near wake of a circular cylinder. *J. Fluid Mech.* **136**, 321–374.

KAWALL, J. G., SHOKR, M. & KEFFER, J. F. 1983 A digital technique for the simultaneous measurement of streamwise and lateral velocities in turbulent flows. *J. Fluid Mech.* **133**, 83–112.

LIM, T. T. 1979 Coherent structures in coflowing jets and wakes. Ph.D. thesis, University of Melbourne.

PERRY, A. E. 1982 *Hot-Wire Anemometry*. Clarendon.

PERRY, A. E., CHONG, M. S. & LIM, T. T. 1982 The vortex shedding process behind two-dimensional bluff bodies. *J. Fluid Mech.* **116**, 77–90.

PERRY, A. E. & LIM, T. T. 1978 Coherent structures in coflowing jets and wakes. *J. Fluid Mech.* **88**, 451–463.

PERRY, A. E., LIM, K. L., HENBEST, S. M. & CHONG, M. S. 1983 Rough- and smooth-walled shear flows. *Presented at the Fourth Symp. on Turbulent Shear flows, Karlsruhe F.R. Germany, September 12–14 1983.*

PERRY, A. E. & STEINER, T. R. 1986 Large-scale structures in turbulent wakes behind bluff bodies. Part 1. Vortex formation processes. *J. Fluid Mech.* **174**, 233–270.

PERRY, A. E. & TAN, D. K. M. 1984 Simple three-dimensional vortex motions in coflowing jets and wakes. *J. Fluid Mech.* **141**, 197–231.

PERRY, A. E. & WATMUFF, J. H. 1981 The phase-averaged large-scale structures in three-dimensional turbulent wakes. *J. Fluid Mech.* **103**, 33–51.

STEINER, T. R. 1984 A study of turbulent wakes and the vortex formation process. Ph.D. thesis, University of Melbourne.

SULLIVAN, R. D. 1959 A two-celled solution of the Navier–Stokes equations. *J. Aero. Sci.* **26**, 767–768.

TUTU, N. K. & CHEVRAY, R. 1975 Cross-wire anemometry in high intensity turbulence. *J. Fluid Mech.* **71**, 785–800.

WATMUFF, J. H. 1979 Phase-averaged large-scale structures in three-dimensional turbulent wakes. Ph.D. thesis, University of Melbourne.